PCCP

Informing Air-Carbon Ablation Modeling with Theoretical Calculations of Atomic Oxygen and Nitrogen Interacting with Carbon Surfaces

Journal:	*Physical Chemistry Chemical Physics*
Manuscript ID	CP-ART-03-2023-001354.R1
Article Type:	Paper
Date Submitted by the Author:	01-May-2023
Complete List of Authors:	Nieman, Reed; Texas Tech University, Dep. Chemistry and Biochemistry Sands, Michael; University of Colorado Wang, Yingqi; University of New Mexico Minton, Tim; University of Colorado at Boulder, Aerospace Engineering Sciences Mussoni, Erin; Sandia National Laboratories Engerer, Jeffrey; Sandia National Laboratories Guo, Hua; University of New Mexico, Department of Chemistry

submitted to PCCP, 3/24/2023, revised 5/1/2023

Informing Air-Carbon Ablation Modeling with Theoretical Calculations of Atomic Oxygen and Nitrogen Interacting with Carbon Surfaces

Reed Nieman,[a,%] Michael Sands,[a,$] Yingqi Wang,[a] Timothy K. Minton,[b] Erin E. Mussoni,[c] Jeffrey Engerer,[d] and Hua Guo[a, *]

[a]Department of Chemistry and Chemical Biology, University of New Mexico, Albuquerque, NM 87131

[b]Ann and H.J. Smead Department of Aerospace Engineering Sciences, University of Colorado, Boulder, CO 80303

[c]Thermal/Fluid Science and Engineering, Sandia National Laboratories, Livermore, CA 94550

[d]Fire Science and Technology, Sandia National Laboratories, Albuquerque, NM 87123

%: current address: Department of Chemistry and Biochemistry, Texas Tech University, Lubbock, TX 79409

$: current address: Department of Chemistry, University of Colorado, Boulder, CO 80309

*: corresponding author, hguo@unm.edu

Abstract:

To understand the gas-surface chemistry above the thermal protection system of a hypersonic vehicle, it is necessary to map out the kinetics of key elementary reaction steps. In this work, extensive periodic density functional theory (DFT) calculations are performed to elucidate the interaction of atomic oxygen and nitrogen with both the basal plane and edge sites of highly oriented pyrolytic graphite (HOPG). Reaction energies and barriers are determined for adsorption, desorption, diffusion, recombination, and several reactions. These DFT results are compared with the most recent finite-rate model for air-carbon ablation. Our DFT results corroborated some of the parameters used in the model but suggest that further refinement may be necessary for others. The calculations reported here will help to establish a predictive kinetic model for the complex reaction network present under hypersonic flight conditions.

I. Introduction

The shock layer on the leading edges of vehicles traveling at hypersonic speeds presents an environment where complex gas-phase and gas-surface interactions take place. Atmospheric oxygen and nitrogen molecules can dissociate to their constituent atomic species,[1, 2] which are much more reactive than their molecular parents. Depending on the application, thermal protection systems consisting of pure carbon materials or carbon-phenolic ablators that char to carbon are commonly used to protect the vehicle from boundary layer temperatures that frequently exceed 5000 K. Reactions between O and N atoms with hot carbon surfaces are thus highly relevant to hypersonic ablation during hypersonic flight. At very high temperatures and pressures, equilibrium chemistry assumptions with instantaneous rates are appropriate, but at lower temperatures (<2000 K) and/or lower pressures corresponding to higher altitude flight, the kinetics must be modeled with finite rates. To couple chemistry with hypersonic fluid dynamics, kinetic models are therefore needed.

Earlier ablation models generally neglected the material chemistry and unique phases of carbon, instead relying on a surface active-site-density parameter that may be calibrated to bulk-scale experimental data.[3-5] Further development of air-carbon-ablation models focused instead on the microscopic mechanisms underpinning the gas-surface chemical processes.[6-8] The most recent finite-rate Air-Carbon Ablation (ACA) model produced by Prata et al.[8] was built upon the oxygen-carbon reaction model of Poovathingal et al.,[6] aided by the latest information provided by high-velocity O, N, and O_2 molecular beam experiments with carbon surfaces.[9-12] This finite-rate model is comprised of ~20 reactions with corresponding *ad hoc* rate coefficients, including gas-surface reactions that are dependent on surface coverage of adsorbed O and N atoms. Simulations based on this model successfully reproduced the observations in the existing molecular beam experiments.

Assessments of finite-rate surface ablation models are important to build evidence to inform model credibility. There are two approaches to assess the validity of the models. One is to test the model's predictions against the available experimental observations. To this end, the model of Prata et al.[8] has been quite successful. An alternative approach is to compare the thermodynamics and kinetics of its constituent elementary reactions to reliable theory. This bottom-up approach has not been attempted so far and is the main motivation of the current work.

There has been a plethora of theoretical and experimental studies on the fundamental interactions between various gaseous species and carbon surfaces, which are summarized below and provide the backdrop for our theoretical investigation reported in this publication.

Because of the relative importance of oxidization reactions, most studies have so far focused on atomic and molecular oxygen (O and O_2) species interacting with carbon surfaces, such as highly oriented pyrolytic graphite (HOPG) and vitreous carbon. Experiments have been performed to investigate these processes over a wide range of conditions (i.e., incident energies and angles, surface temperatures, etc.) where the volatile products and oxidized surfaces offer insight into the underlying chemical and physical processes.[9, 10, 12-17] In the molecular beam studies of Murray et al.,[9, 10, 12] hyperthermal scattering of O and O_2 with carbon surfaces led to scattering of the incident species and several reaction products such as O_2, CO, and CO_2, with CO as the major reaction product. Molecular oxygen was shown to be largely an inert species, as evidenced by near specular scattering angles, but the scattered O_2 also bears signatures of O-atom recombination.

Experiments have also explored N and N_2 interactions with carbon surfaces. Molecular nitrogen is inert, but reactions involving atomic nitrogen have been documented for several decades.[18-23] Recent molecular beam experiments provide valuable information on N atom and N_2 scattering from carbon,[11, 12] showing that, in addition to direct scattering of the two species, there was evidence of N atom recombination forming N_2 and reactions producing CN. Finally, there was also evidence of temperature dependent trapping of atomic nitrogen at the surface in which the N atoms stick to the surface at lower temperatures and desorb at higher surface temperatures.[12]

Theoretical simulations and modeling provide microscopic details of the mechanistic processes underpinning the observed reactions. Interactions of O and O_2 with HOPG surfaces have been extensively investigated theoretically, mostly using various density functional theory (DFT) methods. The weak interaction of O_2 with the defect-free basal plane of pristine graphene/graphite is well-established,[24-27] while it has also been shown that reactions of O_2 at defect sites leads to dissociation and subsequent oxidation.[16, 28, 29] Atomic oxygen, on the other hand, can chemically bind to bridge sites on pristine carbon surfaces forming an epoxide group.[30, 31] Depending on the level of theory, the calculated adsorption energy is found to vary from -0.95 to -3.20 eV.[32-35] The calculated diffusion barrier on a graphene surface ranges from 0.40 to 0.76 eV,[32, 35-37] in agreement

with experimental observation of O migration on HOPG.[38] Morón et al. also detailed the mechanisms for several reaction pathways such as the formation of O_2 via the Langmuir-Hinshelwood (LH) mechanism, featuring a large energy barrier of about 1.28 eV.[35] The formation dynamics of O_2 via the Eley-Rideal (ER) mechanism was investigated via trajectories and found to be facile.[39] The formation of CO and CO_2 has also been investigated theoretically.[40, 41] Direct dynamics simulations of hyperthermal atomic oxygen scattering from defect-free and defected basal planes of HOPG have revealed various products such as O_2, CO, and CO_2.[15, 42-45]

There have also been extensive theoretical investigations of nitrogen-graphite/graphene surface interactions involving N_2 and N.[46-56] Plane-wave DFT calculations performed by Wang et al.[56] investigated the adsorption and desorption of an N atom on HOPG. The adsorption energy was determined to be 1.1 eV at the bridge site and the migration of an N atom was found to have a barrier of 0.88 eV. Recombination of two N atoms on the surface to form N_2 was found to proceed through a relatively low barrier of 0.53 eV via an LH mechanism. The formation of N_2 was found to be barrierless when proceeding via an ER mechanism. Direct dynamics simulations of hot N impinging on HOPG (with and without surface oxygen coverage) observed several products such as CN and NO,[55] as well as a corresponding surface morphology change.[57]

In this work, we examine several key gas-surface interactions identified in the ACA model of Prata et al.[8] using periodic DFT. Our theoretical models provide a consistent and uniform platform to assess the parameters used in the model. Various reaction sites on HOPG are examined and the calculated reaction energies and barriers are used to assess the validity of the parameters in the model. These calculated properties may be leveraged to create a more comprehensive and predictive model based solely on first principles results. Although this goal is highly desired, it is not attempted in the present work.

II. Computational Details

The adsorption and reactivity of O and N atoms with HOPG were investigated utilizing a first principles method based on periodic DFT. This method has the benefit of being computationally efficient while achieving improved accuracy and reliability over force field-based interaction potentials and methods based on semi-empirical Hamiltonians.

Two types of surface morphologies were constructed to represent ablating carbon surfaces: basal and edge planes. The basal plane was modeled with a $p(5\times5)$ unit cell in a slab containing a single layer graphene sheet, which provides a reasonable representation of the HOPG basal plane. On the other hand, the edge plane was modeled with a slab containing four truncated graphene layers. Edge-plane simulations included both the armchair (AC) and zigzag (ZZ) edge sites. Since the exact edge composition of carbon ablators is mostly unknown with respect to functionalization, the edge sites utilized in this work were pacified with hydrogen, which is common in other computational studies investigating reactions at AC and ZZ edges. Vacuum layers of 30.0, 15.6, and 18.9 Å between the slabs were utilized for the basal plane model, ZZ edge, and AC edge, respectively. The exemplary unit cells of these models are shown in Figure 1. The valence electron density was expanded in a plane-wave basis with a cutoff energy of 400 eV, and the projector augmented wave (PAW) scheme[58] was used to approximate the electron-ion interaction. A 1 × 1 × 1 Monkhorst-Pack *k*-point mesh[59] was used for the Brillouin zone integration. All DFT calculations were spin-polarized. Convergence of the self-consistent field (SCF) energy was determined with a tolerance of less than 10^{-5} eV, while for geometry optimizations, convergence was reached when the force on each atom was less than 0.05 eV/Å. All DFT calculations were performed with the Vienna *Ab initio* Simulation Package (VASP).[60, 61]

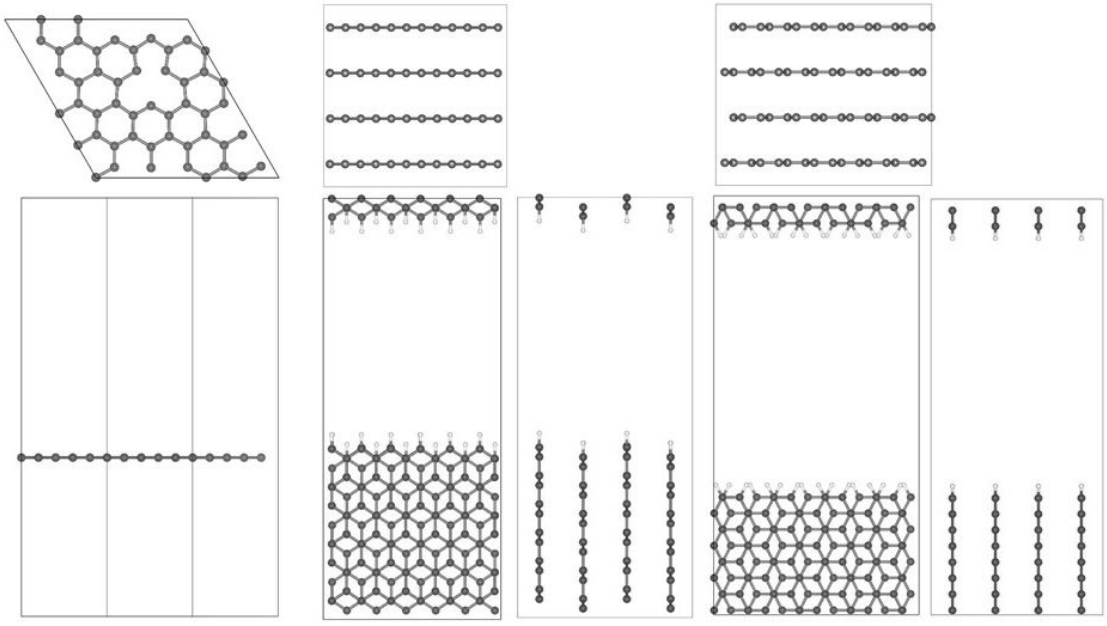

Figure 1. Unit cells for the basal plane (pristine and with SV), zigzag edge, and armchair edge, respectively.

For the edge site structures, it is important to accurately model the van der Waals (vdW) forces between the layers. For this reason, the DFT calculations utilized the optimized Perdew-Burke-Ernzerhof (optPBE) exchange-correlation functional,[62] and the vdW density functional (vdw-DF).[63] For the latter, the exchange-correlation energy consists of local and non-local correlations to account for the dispersion forces. This choice is motivated by its ability to reproduce the interlayer distances of graphite, as discussed in Supporting Information (SI).

The adsorption energy of a given adsorbate was calculated as:

$$E_{ad}(adsorbate) = E_{adsorbate/surface} - E_{adsorbate} - E_{surface} \quad (1)$$

where $E_{adsorbate/surface}$ is the total energy of the adsorbate on the surface, $E_{surface}$ is the total energy of the clean surface, and $E_{adsorbate}$ is the total energy of the gas phase adsorbate. To further test the functional, adsorption energies of O and N on the basal plane of HOPG are determined using a smaller p(4x4) unit cell with a hybrid functional (HSE06).[64] The HSE06 results are 0.49 and 0.43 eV smaller than the optPBE and functional for E_{ad}(O) and E_{ad}(N), respectively. These results suggest that the PBE functional generally overestimates the adsorption energy.

Transition states (TSs) were determined between the initial state (IS) and final state (FS), utilizing the climbing image-nudged elastic band (CI-NEB)[65] and dimer methods.[66] The convergence criteria for the energy and forces were the same as those used in geometry optimization. The Hessian matrix of the stationary points was calculated to obtain the harmonic vibrational frequencies of the vibrational modes, which confirm their stationary nature. The activation energy or reaction barrier for an elemental process is defined as

$$E_A = E_{TS} - E_{IS}, \quad (2)$$

while the corresponding reaction energy is given by

$$\Delta E_{RXN} = E_{FS} - E_{IS}. \quad (3)$$

In results presented below, all energy values are reported with zero-point energy correction.

Finally, we note that DFT results depend on many factors in the computation, such as the type and size of the model, the functional used, and parameters in the calculation. More importantly, there is no systematic way to improve the results. As a result, the DFT results may contain significant uncertainties.

III. Results and Discussion

A. Oxygen-HOPG interaction

The adsorption of atomic oxygen on the defect-free graphene basal plane is calculated using the model described in Sec. II. The most stable adsorption site is at a bridge site, forming a three-membered epoxide species, as shown in Figure 2. The corresponding C-O bonds have a length of 1.479 Å, while the C-C bond is elongated from the equilibrium length of 1.420 Å to 1.507 Å. The calculated optPEB adsorption energy is -2.11 eV, which is in general agreement with previous DFT results using various functionals.[30-35] We have also simulated the adsorption of atomic oxygen on a defected basal surface, using a single carbon vacancy (SV) to represent the defect. The adsorption configuration is also shown in Figure 2 and the C-O bond length of 1.234 Å suggests a carbonyl species. The adsorption energy of -5.97 eV is significantly larger than the defect-free case mentioned above, and consistent with that reported by Mehmood et al. (-7.58 eV) using the PBE functional.[37]

The adsorption of atomic oxygen on an AC and a ZZ edge site has also been examined using the models outlined in Sec. II. Here, the carbon site that receives the incoming O atom is assumed to be unsaturated, while the rest of the edge plane is terminated by hydrogen. The adsorption configurations are shown in Figure 2. In both cases, the adsorption energy is quite large: -6.36 eV for AC and -7.32 eV for ZZ. Lopez-Urias et al. found using the PBE functional the desorption energy of O from the AC site to be somewhat smaller at 4.78 eV.[67] The C-O bond length is 1.274 and 1.247 Å, respectively, suggesting again a carbonyl species.

In the ACA model,[8] two scenarios were considered for O-atom adsorption to a carbon surface: weakly adsorbed O atoms (denoted as O), and strongly adsorbed O atoms (denoted as O*). The former was assumed to be for carbon-oxygen single bonds and the latter for carbon-oxygen double bonds. Based on our optPBE calculations, we have interpreted the former as

adsorption of O at a bridge site on the defect-free basal plane, while the latter as adsorption at a defect or edge site (AC, ZZ, or SV).

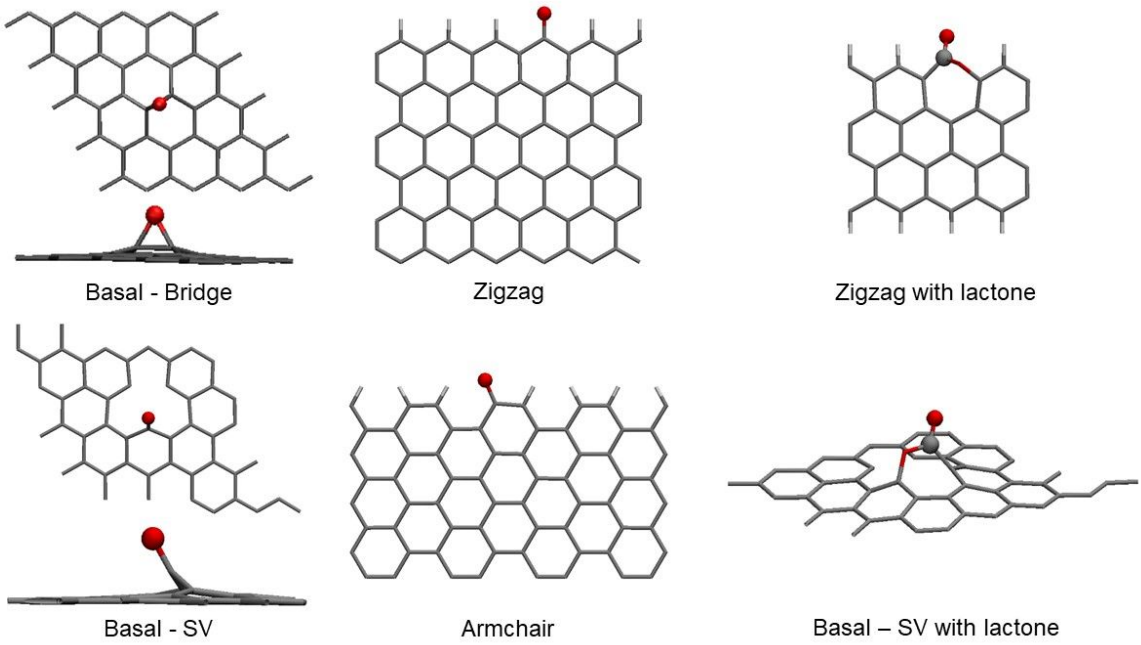

Figure 2. O-atom adsorption configurations on the basal plane bridge site, SV defect, ZZ edge, AC edge, ZZ edge with lactone group, and basal plane SV defect with lactone group, respectively. For the edge sites, only one graphene sheet is shown.

The adsorption/desorption pathways for atomic oxygen were investigated for the four adsorption sites (defect-free SV, AC, and ZZ), and no saddle point was found in all cases. As a result, the negative adsorption energies can be considered as the desorption barriers, which are listed in Table 1. Comparing with the activation energies of 3.82 and 8.32 eV for the O and O* species in the ACA model,[8] our optPBE desorption barriers of 2.11 and 5.97/6.36/7.32 eV support the existence of two different O adsorption states. Quantitatively, the ACA model value of 3.82 eV for the weaker O atom desorption is about 1.7 eV larger than the optPBE value for an epoxide structure on the basal plane, and the stronger O* atom value is about 1.0 eV larger than that for the O atom of a carbonyl group of the ZZ site. The overestimation is even larger for other defect sites studied here.

Table 1: Comparison of reaction energies ($\Delta E_{RXN,\,DFT}$) and activation energies ($E_{A,\,DFT}$), calculated using the optPBE functional, with activation energies from the ACA model ($E_{A,\,Model}$)[8] for oxygen-related reactions. The surface type is given in parentheses: defect-free basal plane (basal), basal plane with a single carbon vacancy defect (SV), armchair configuration of the edge plane (AC), and zigzag configuration of the edge plane (ZZ). LH stands for the Langmuir-Hinshelwood mechanism.

	$\Delta E_{RXN,\,DFT}$ (eV)	$E_{A,\,DFT}$ (eV)	$E_{A,\,Model}$ (eV)
O adsorption	-2.11 (basal)	0.0 (basal)	0.0
O desorption	2.11 (basal)	2.11 (basal)	3.82
O* adsorption	-5.97 (SV)	0.0 (SV)	0.0
	-6.36 (AC)	0.0 (AC)	
	-7.32 (ZZ)	0.0 (ZZ)	
O* desorption	5.97 (SV)	5.97 (SV)	8.32
	6.36 (AC)	6.36 (AC)	
	7.32 (ZZ)	7.32 (ZZ)	
O mediated CO desorption	-	-	0.35
O* med. CO desorption	-0.85 (SV)	0.92 (SV)	0.35
	-0.72 (ZZ)	1.26 (ZZ)	
2 O(s) → O_2, LH	-1.82 (basal)	0.91 (basal)	1.29
2 O*(s) → O_2, LH	6.52 (AC)	6.52 (AC)	1.29
	8.00 (ZZ)	8.00 (ZZ)	
O_2 → 2 O(s)	1.82 (basal)	2.73 (basal)	0.69
O_2 → 2 O*(s)	-6.52 (AC)	0.0 (AC)	0.68
	-8.00 (ZZ)	0.0 (ZZ)	

The formation of CO has been identified as a major product channel in molecular-beam experiments[9, 10, 12] and this observation was reproduced by the ACA model.[8] As a result, we have systematically investigated the reaction pathways leading to the formation of CO products. On the defect-free basal plane, the formation of CO from adsorption of O is extremely difficult because it breaks several bonds, as shown in previous experimental[38] and theoretical studies.[44, 45] However, it is conceivable for CO formation at a defect site on the basal plane. In our model, this defect site

was simulated as the same SV site described above and a CO species is assumed to exist at the site. The configuration of the surface bound carbonyl species at the SV defect is shown in Figure 2. The desorption of CO from this configuration was simulated and the energy profile is displayed in Figure 3, which features a saddle point serving as the TS. At the TS, the C-O bond length is shortened from 1.23 at IS to 1.18 Å, while the C-C bond length changes from 1.48 to 1.59 Å. At FS, the C-O and C-C bond lengths are 1.14 and 4.06 Å, respectively. The optPBE reaction energy for the desorption process is 2.30 eV, with a barrier of 3.28 eV. The existence of a desorption barrier is known from the molecular beam experiments.[10] The edge site, which is modeled as ZZ, also features a carbonyl species, as shown in Figure 2. The optPBE desorption energetics are also shown in Figure 3, which has a reaction energy of 4.11 eV and a barrier of 4.11 eV. The C-O bond length is shortened from 1.25 Å at IS to 1.14 Å at TS, while the C-C bond length changes from 1.49 to 4.57 Å. The C-O and C-C bond length at FS are 1.142 and 3.888 Å, respectively.

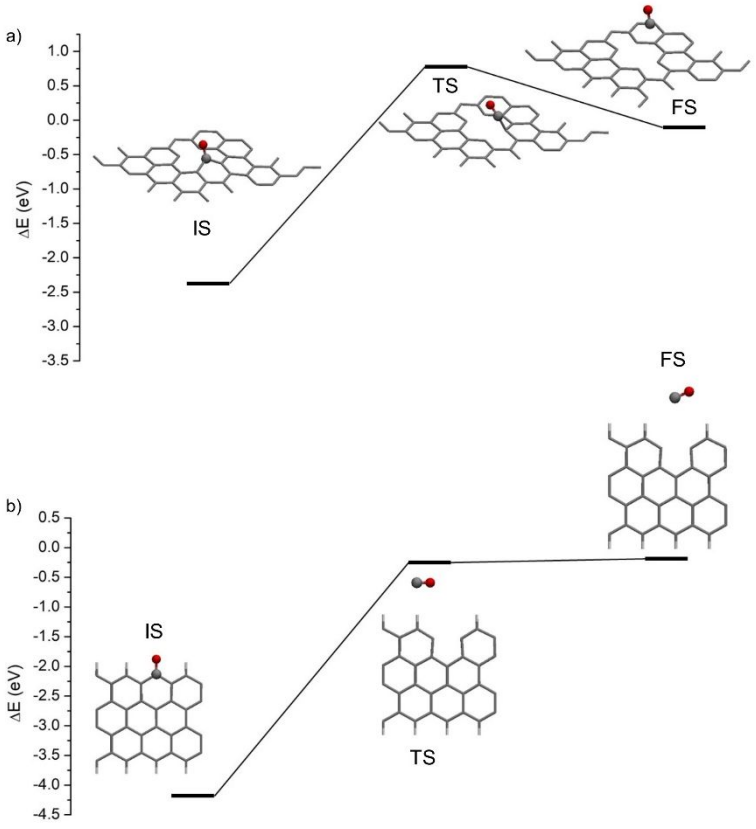

Figure 3. Energy profiles for CO desorption from a) an SV defect on the basal plane and b) from the ZZ edge. Associated geometry configurations are provided for the IS, TS, and FS.

In the ACA model,[8] the formation of CO is assumed to be mediated by additional incident gas-phase O atoms, which activate the desorption of CO from preexisting surface-adsorbed O atoms (O and O* mediated CO desorption in Table 1). A similar mechanism was also adapted in the finite-rate model of Poovathingal et al.[6] There is strong experimental evidence in support of this mechanism, as the flux of CO leaving the surface was found to be greater at lower temperatures when the surface coverage of O atoms was higher, but the flux decreased with increasing surface temperature as the surface O coverage decreased.[10] As a result, the sole CO desorption mechanism discussed above is probably only relevant at the zero O coverage limit. To better understand the effect of nearby adsorbed oxygen atoms on the desorption of CO, we have carried out additional calculations. In the SV case, optPBE simulations showed that higher surface oxygen coverages, modeled by additional oxygen adsorbates in nearby sites, lower the barrier for CO desorption, as shown in Figure S1 in SI. The effects of nearby oxygen atoms are similar to those reported earlier by Sun et al.[40] who found using the PBE functional a reduction of the CO formation barrier from 1.86 to 0.50 eV with increasing surface oxygen coverage on defected basal graphene. The additional oxygen in the form of lactone groups (shown in Figure 2) is particularly effective, as illustrated by the reaction energetics in Figure 4. The optPBE barrier for CO desorption is reduced from 3.28 eV in the absence of the extra oxygen to 0.92 eV with the lactone group. For the O* atom at the ZZ edge site, a lactone group (Figure 2) analogously reduces the barrier to CO desorption from 4.11 to 1.26 eV. The reduction of the barrier is accompanied with the change of the reaction energy from 4.11 to -0.72 eV, presumably due to the stabilization of the FS by the additional oxygen adsorbate, which forms an ether bond with the two nearby carbon atoms. It is interesting to note that the lactone group was found to be an important precursor toward CO desorption in previous direct dynamics studies.[15, 44, 45] So the optPBE results presented here provide a convincing rationalization of the previous results. The optPBE barrier for CO desorption, 0.92 (SV) and 1.26 (ZZ) eV, are higher than the value used in the ACA model (0.35 eV). On the other hand, they are closer to the experimental estimations of the barrier of ~1.25 ± 0.05 and ~1.61 ± 0.07 eV at 1100 and 1300 K, respectively.[10]

Reactions forming CO_2 are also included in the ACA model,[8] however, as they are identified as a minor product forming pathway in the experiment,[9, 10, 12] these reactions were not part of the present investigation.

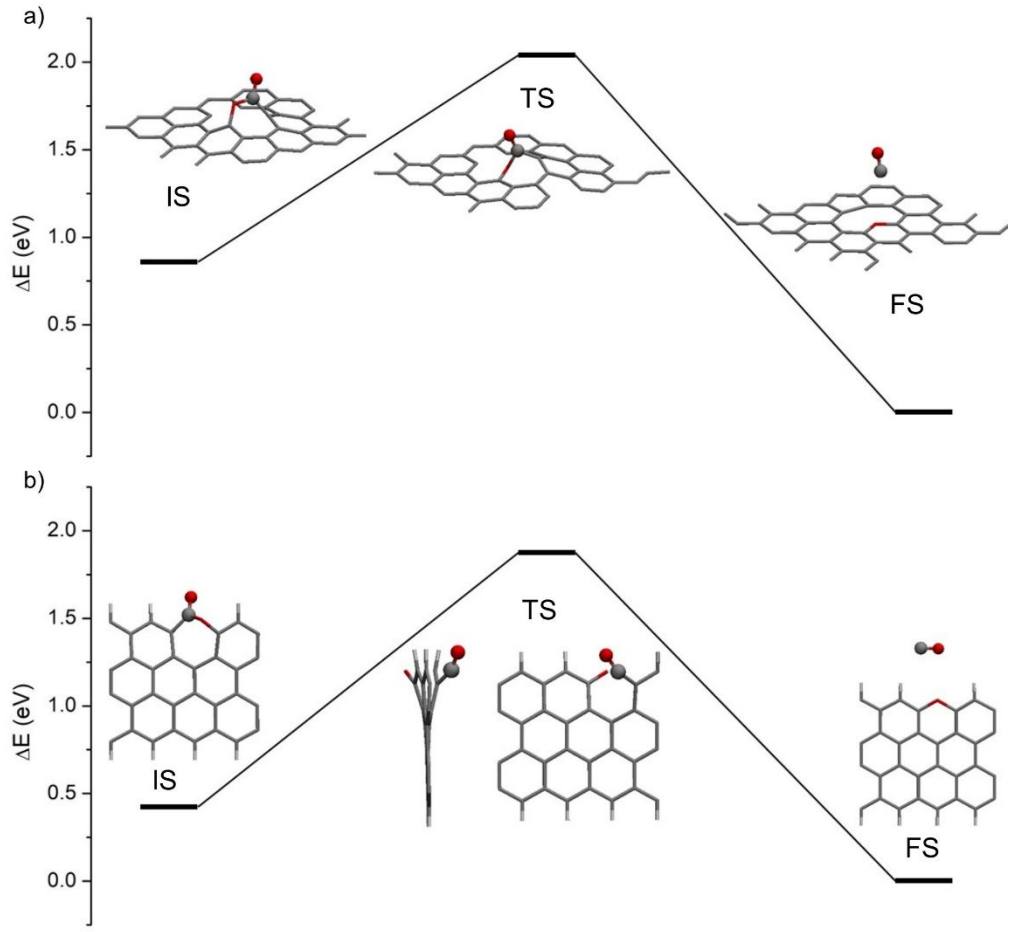

Figure 4: Energy profiles for CO desorption from a lactone group at a) an SV defect on the basal plane and b) at the ZZ edge. Associated geometry configurations are provided for IS, TS, and FS.

The recombinative desorption of surface adsorbed O atoms through an LH mechanism is believed to be an important process,[12] and such events both deplete surface coverage and release energy to the surface. However, O-O recombination also competes with CO production. To account for this competition, particularly at higher temperatures where recombination is more

important, the ACA model included the recombination reaction.[8] We have examined this LH reaction using DFT. For weakly-bound O atoms, as shown in Figure 5, recombination on the basal plane proceeded from two adjacent O adsorbates separated by 2.88 Å to a TS with a much-shortened O-O distance of 2.11 Å. As expected, this process is exoergic with a reaction energy of -1.82 eV. The barrier was found to be 0.91 eV, which can be compared with the previous theoretical value of 1.28 eV determined by Morón et al. using the RPBE functional.[35] As shown Table 1, the value adapted by the ACA model is 1.29 eV.[8]

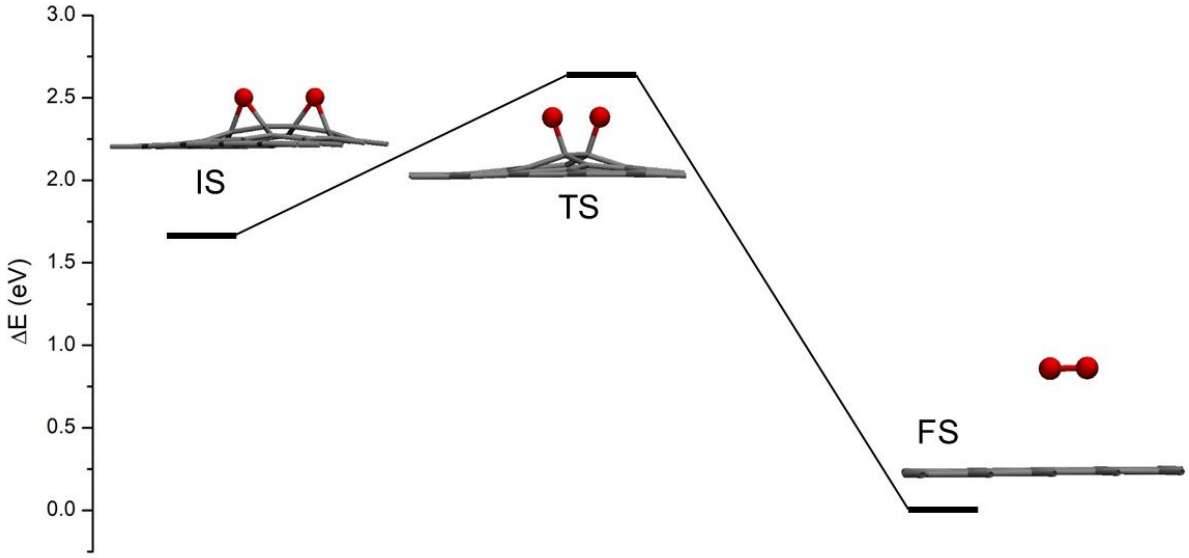

Figure 5: Reaction profile of the recombinative desorption of O_2 on the defect-free basal plane. Associated geometry configurations are provided for IS, TS, and FS.

When considering the recombinative desorption of strongly-bound O* atoms, modeled at edge sites, our calculations find that the process becomes highly endoergic. This can be attributed to the breaking of essentially two C=O double bonds and formation of only one O=O double bond. Specifically, our calculations considered AC and ZZ edge types, as the SV site is too small to accommodate two C=O groups. The optPBE results for the formation of O_2 on these two sites found no saddle points and as a result the recombinative desorption barrier of O_2 is the same as the

reaction energies: 6.52 and 8.00 eV, respectively. These values are much larger than the E_A value (1.29 eV) in the ACA model,[8] which was set to be the same as that of the weakly bound O atom reaction.

The dissociation of gas-phase O_2 into adsorbed O/O* species on HOPG is simply the reverse process of recombinative desorption. For the defect-free basal plane, the optPBE dissociation barrier is 2.73 eV, as shown in Figure 5. Earlier theoretical work by Morón et al.,[35] using the RPBE functional, predicted the reaction energy and barrier height to be 3.23 and 4.51 eV, respectively, which are much larger than our results. The quantitative differences may stem from the small unit cell size utilized in their work corresponding to a higher surface coverage. The E_A value utilized by the ACA model[8] is much smaller than either set of results, however, at only 0.69 eV, almost 2 eV less than our optPBE value for the barrier. The ACA model E_A value for recombination of O atoms to form O_2 is larger than that for the dissociation of O_2 at the surface, which implies the dissociation is an exothermic process. Hence, the ACA model is in contradiction to our optPBE results and the experimental observation that O_2 is essentially an inert species in hyperthermal gas-surface scattering.[9, 10, 12]

Our optPBE results indicate that the dissociation of the impinging O_2 molecule at the AC and ZZ edge sites is exothermic and proceeds without a barrier, provided that the carbon edge sites are unsaturated, as shown in Figure S2 of SI. Derived from the results for recombinative desorption as discussed above, the calculated reaction energies at AC and ZZ edge sites are -6.52 and -8.00 eV, respectively. Previous DFT calculations at the ZZ edge site performed by Sendt and Haynes using the B3LYP functional found a barrier of 0.03 eV and a reaction energy of -3.42 eV.[68] The E_A value in the ACA model is 0.68 eV,[8] the same as the dissociation to weakly bounded O atoms.

Diffusion of an adsorbed O atom from one bridge site to an adjacent bridge site on the basal plane was treated as barrierless in the ACA model by Prata et al.,[8] which assumed that the adsorbed O atoms behave like a two-dimensional ideal gas. Our optPBE calculation yielded a value of 0.69 eV for the diffusion barrier, which is quite high, indicating that O atoms are not mobile on the surface except at high temperatures. This value is in good agreement with Sun et al.[40] who reported using the PBE functional 0.72 eV. The transition state for diffusion features an O bond at an atop site, as shown in Figure 6. The high diffusion barrier casts some doubt on the treatment of adsorbed

O atoms on HOPG as a two-dimensional gas. We did not consider the migration of O between edge sites, as the barrier is expected to be quite high due to the strong C=O bonds.

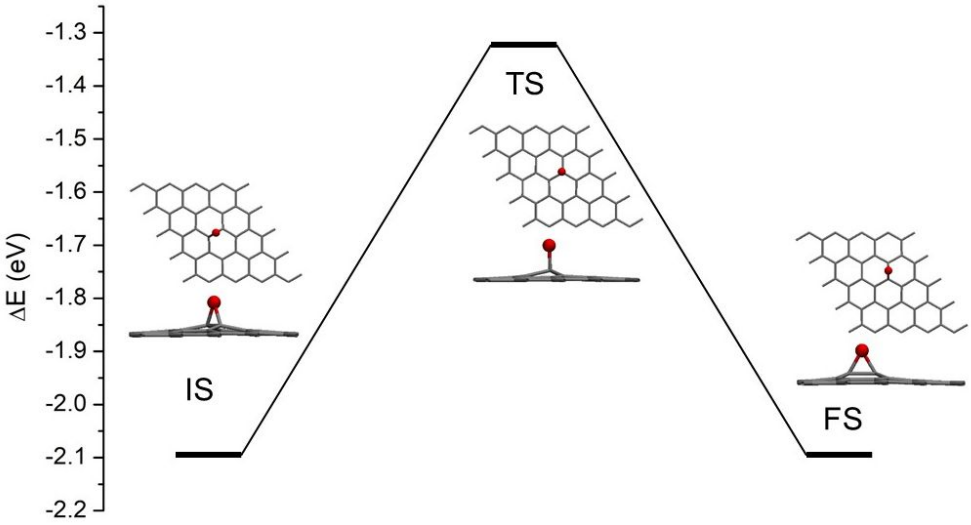

Figure 6: Reaction profile of the diffusion of a weakly-bound O atom on the defect-free basal plane of HOPG. Associated geometry configurations are provided for IS, TS, and FS.

B. Nitrogen-HOPG interaction

Comprehensive DFT calculations using the optB86b-vdW-DF functional were performed recently by Wang et al.[56] to understand N-atom adsorption and diffusion on the basal plane of HOPG as well as recombination to form N_2. These optPBE results are compared to the activation energies from the ACA model of Prata et al.[8] in **Error! Reference source not found.**. The optPBE adsorption energy of an N atom on the defect-free basal plane of HOPG was determined to be -0.75 eV, in reasonably good agreement with our previously determined optB86b-vdW-DF value of -1.10 eV[56] and another previous value of -0.93 eV reported by Pašti et al. using the PBE functional.[54] As Figure 7 shows, the adsorption geometry at a bridge site features a three-membered ring similar to the epoxide structure of oxygen, but the adsorption energy is significantly smaller than that of an O atom (-2.11 eV). In addition, there is a physisorption well with a depth of -0.16 eV. The adsorption pathway, shown in Figure 8, has a small (0.40 eV) barrier

from the physisorption, which is 0.19 eV below the asymptote. This compares favorably to the E_A of the ACA model, 0.22 eV.[8]

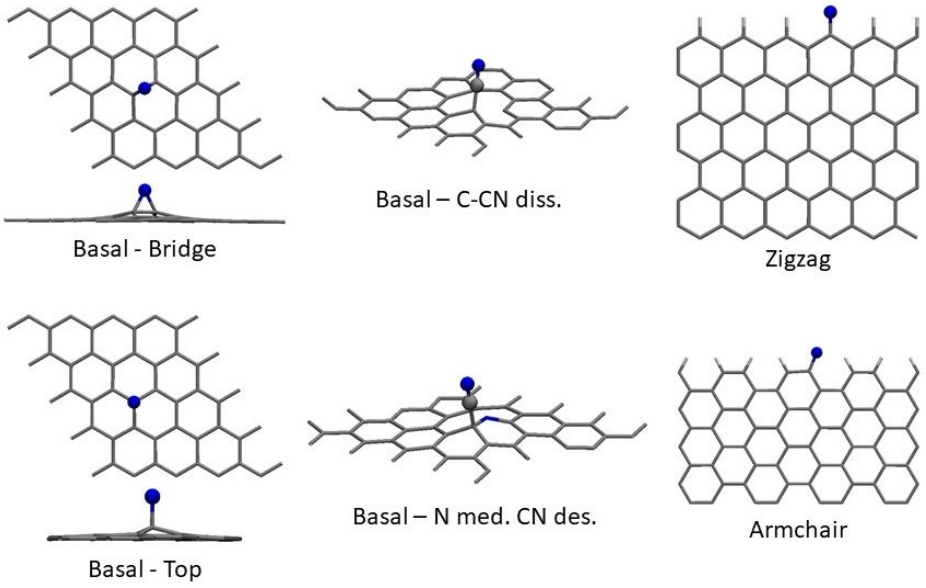

Figure 7: N atom adsorption configurations on basal plane, at the AC edge, and at the ZZ edge. Also included are the initial configurations for the removal of CN from the basal plane at the SV defect.

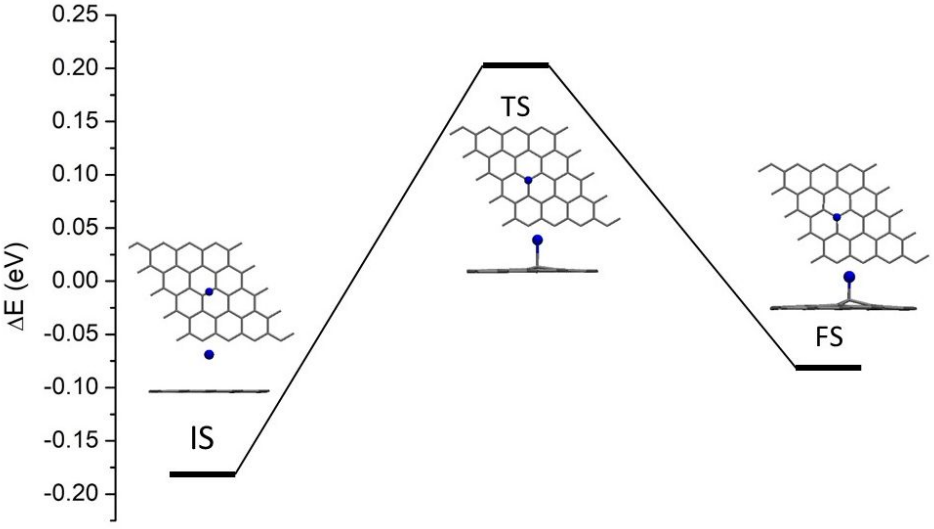

Figure 8: Reaction profile for the adsorption/desorption of N atoms on the basal plane of HOPG. Associated geometry configurations are provided for IS, TS, and FS. Note that the IS is the physisorption state for N on HOPG, which is -0.19 eV below the reactant asymptote.

The adsorption of atomic nitrogen at edge sites has been investigated here using the optPBE functional. As in the oxygen case, the edge carbon is assumed to be initially unsaturated in our calculations. The optPBE adsorption energies are -4.76 and -5.77 eV for the AC and ZZ cases, respectively, which are much larger than that on the basal plane. Indeed, the C-N bond length is 1.310 and 1.280 Å for the AC and ZZ sites, respectively, suggesting double bonds. The corresponding geometries of these adsorption species are shown in Figure 7. Additionally, no saddle point was found between the IS and FS. The corresponding desorption barriers, 4.76 and 5.77 eV, can be compared with the barrier (6.37 eV) used in the ACA model.[8] Our optPBE results suggest that the N species in the ACA model does not correspond to the adsorption at the defect-free basal plane of HOPG. Rather, it is most likely attributable to the strongly bound N at edge sites (or at a defect site on the basal plane).

Table 2: Comparison of reaction energies ($\Delta E_{RXN,\,DFT}$) and activation energies ($E_{A,\,DFT}$), calculated using the optPBE functional, with activation energies from the ACA model ($E_{A,\,Model}$)[8] for nitrogen reactions. Units are in eV. The adsorption site is given in parentheses: bridge and top sites on defect-free basal plane (basal bridge/top), basal plane with single carbon vacancy defect (SV), armchair configuration of the edge plane (AC), and zigzag configuration of the edge plane (ZZ). Basal plane results were adapted from Wang et al.[56] ER or LH stand for the Eley-Rideal or Langmuir-Hinshelwood mechanisms, respectively.

	$\Delta E_{RXN,\,DFT}$ (eV)	$E_{A,\,DFT}$ (eV)	$E_{A,\,Model}$ (eV)
N adsorption	-0.75 (basal, bridge)	0.19 (basal, bridge)	0.22
	-0.13 (basal, top)	0.40 (basal, top)	
	-4.76 (AC)	0.0 (AC)	
	-5.77 (ZZ)	0.0 (ZZ)	
N desorption	0.75 (basal, bridge)	0.75 (basal, bridge)	6.37
	0.13 (basal, top)	0.25 (basal, top)	
	4.76 (AC)	4.76 (AC)	

	5.77 (ZZ)	5.77 (ZZ)	
CN desorption	2.34 (SV)	2.34 (SV)	1.78
N mediated CN desorption	0.73 (SV)	0.73 (SV)	0.60
$N(g) + N(s) \rightarrow N_2$, ER	-9.68 (basal)	0.0 (basal)	0.17
$2\ N(s) \rightarrow N_2$, LH	-8.35 (basal)	0.53 (basal)	1.81

The production of gaseous CN has been observed in molecular beam scattering studies of N-atom interactions on a vitreous carbon surface.[11, 12] This process is simulated using DFT on an SV site of the basal plane. The optimized cyano-group geometry at the SV site is shown in Figure 7, which resembles the carbonyl group at the same site shown in Figure 2. The desorption of the CN group by cleaving the C-C bond is endoergic by 2.34 eV, but with no saddle point along the reaction pathway. This result is in reasonable agreement to our previous result of 2.75 eV using the opt86B functional [56] and is somewhat higher than the activation energy for CN production of 1.78 eV obtained from the most recent molecular beam experiment of Murray et al,[12] which is the value that was used for the ACA model.[8]

We have also investigated the CN desorption with a nearby N atom on the HOPG basal plane. The optimized structure of such a configuration is also shown in Figure 7. The inclusion of an additional N is found to aid the CN desorption, with the corresponding endoergicity lowered from 2.34 eV to 0.73 eV. This behavior is similar to that observed in CO production with nearby O atoms discussed above. No saddle point was found for this process, so the desorption barrier is 0.73 eV, which can be compared with the value of 0.60 eV used in the ACA model.[8]

Recombination forming gaseous N_2 via the ER and LH mechanisms has been included in the ACA model.[8] Although only an LH mechanism for N_2 recombination has been confirmed experimentally,[11] both mechanisms were necessary for consistent comparisons to a wide range of pressure conditions. For the ER mechanism, our previous calculations show with the optB86b functional showed that there is no barrier towards recombination, and the reaction energy was -9.68 eV.[56] A small ER barrier of 0.17 eV was utilized in the ACA model.[8] The reaction energy for the LH mechanism was found to be -8.35 eV and the barrier is 0.53 eV in our previous work with the optB86b functional.[56] Ma et al. found a barrier of 0.80 eV for this reaction using the PW91

functional.[47] The E_A value utilized in the ACA model was 1.81 eV,[47] much larger than the DFT barriers. In addition to the reaction barrier in the LH mechanism, the diffusion of adsorbed N could impact the kinetics. The calculated diffusion barrier for adsorbed N through a top site on the surface is 0.88 eV using the optB86b functional,[56] which is slightly higher than the LH barrier. The diffusion was not considered in the ACA model as the N atoms are treated as two-dimensional gas. This approximation might be appropriate at high enough temperatures, but is questionable at low temperatures.

IV. Conclusions

Accurate finite-rate models are essential for guiding the design and predicting the performance of TPSs for hypersonic vehicles. So far, models have relied on an educated choice of elementary reactions with kinetic parameters determined by reproducing existing experimental data. Given the empirical nature of these models, it is important to validate the parameters used in these models against the best theory for elementary processes. Unlike the gas-phase reactions, where definitive kinetic data are often available, gas-surface interactions are complex and depend on many more factors such as surface coverage, defects, and substrate morphology. In this work, we examined the key elementary steps included in the most recent air carbon ablation model of Prata et al.,[8] using periodic density functional theory. Reaction energies and barriers are determined for several HOPG models and are compared with the parameters in the model. We emphasize that the theoretical results reported here do not consider the complexity engendered in real conditions, yet they serve as a semi-quantitative guide to assess the reasonableness of kinetic parameters. Our theoretical results validated some parameters in the model but suggest further refinement for others. The ultimate kinetic model would have to be based on a network of necessary gas-phase and gas-surface elementary reactions with accurately determined rate coefficients. While this is a challenging goal, the theoretical results presented here provide constraints for future improvements of finite-rate models for air carbon ablation.

Acknowledgements: This work was supported by the Sandia National Laboratories through the Academic Alliance program at University of New Mexico (Grant No. 2312907 to H. G.) and

through a grant to the University of Colorado Boulder (Award No. AWD-21-09-0217 to T. K. M.). Partial support from NASA (Grant No. 80NSSC21K1117 to H.G.) is also acknowledged. Sandia National Laboratories is a multimission laboratory managed and operated by National Technology & Engineering Solutions of Sandia, LLC, a wholly owned subsidiary of Honeywell International Inc., for the U.S. Department of Energy's National Nuclear Security Administration under contract DE-NA0003525. This paper describes objective technical results and analysis. Any subjective views or opinions that might be expressed in the paper do not necessarily represent the views of the U.S. Department of Energy or the United States Government. The calculations were performed at the Center for Advanced Research Computing (CARC) at UNM. We thank Prof. Tom Schwartzentruber for stimulating discussions.

References:

1. P. R. Mahaffy, M. Benna, T. King, D. N. Harpold, R. Arvey, M. Barciniak, M. Bendt, D. Carrigan, T. Errigo, V. Holmes, C. S. Johnson, J. Kellogg, P. Kimvilakani, M. Lefavor, J. Hengemihle, F. Jaeger, E. Lyness, J. Maurer, A. Melak, F. Noreiga, M. Noriega, K. Patel, B. Prats, E. Raaen, F. Tan, E. Weidner, C. Gundersen, S. Battel, B. P. Block, K. Arnett, R. Miller, C. Cooper, C. Edmonson and J. T. Nolan, *Space Sci. Rev.*, 2015, **195**, 49-73.
2. F. S. Milos and Y. K. Chen, *J. Spacecr. Rockets*, 2010, **47**, 786-805.
3. C. Park, *AIAA J.*, 1976, **14**, 1640-1642.
4. S. V. Zhluktov and T. Abe, *J. Thermophys. Heat Transf.*, 1999, **13**, 50-59.
5. C. R. Alba, R. B. Greendyke and J. Marschall, *J. Spacecraft Rockets*, 2016, **53**, 98-120.
6. S. Poovathingal, T. E. Schwartzentruber, V. J. Murray, T. K. Minton and G. V. Candler, *AIAA J.*, 2017, **55**, 1644-1658.
7. K. Swaminathan-Gopalan, A. Borner, V. J. Murray, S. Poovathingal, T. K. Minton, N. N. Mansour and K. A. Stephani, *Carbon*, 2018, **137**, 313-332.
8. K. S. Prata, T. E. Schwartzentruber and T. K. Minton, *AIAA J.*, 2021, **60**, 627-640.
9. V. J. Murray, B. C. Marshall, P. J. Woodburn and T. K. Minton, *J. Phys. Chem. C*, 2015, **119**, 14780-14796.
10. V. J. Murray, E. J. Smoll and T. K. Minton, *J. Phys. Chem. C*, 2018, **122**, 6602-6617.
11. V. J. Murray and T. K. Minton, *Carbon*, 2019, **150**, 85-92.
12. V. J. Murray, P. Recio, A. Caracciolo, C. Miossec, N. Balucani, P. Casavecchia and T. K. Minton, *Carbon*, 2020, **167**, 388-402.
13. H. Kinoshita, M. Umeno, M. Tagawa and N. Ohmae, *Surf. Sci.*, 1999, **440**, 49-59.
14. K. T. Nicholson, T. K. Minton and S. J. Sibener, *J. Phys. Chem. B*, 2005, **109**, 8476-8480.
15. J. T. Paci, H. P. Upadhyaya, J. Zhang, G. C. Schatz and T. K. Minton, *J. Phys. Chem. A*, 2009, **113**, 4677-4685.
16. R. Edel, T. Grabnic, B. Wiggins and S. J. Sibener, *J. Phys. Chem. C*, 2018, **122**, 14706-14713.
17. Z. Zhao, Y. Wang, X. Yang, J. Quan, B. C. Krüger, P. Stoicescu, R. Nieman, D. J. Auerbach, A. M. Wodtke, H. Guo and G. B. Park, *Nat. Chem.*, 2022, **accepted**.
18. C. F. Cullis and J. G. Yates, *Trans. Faraday Soc.*, 1964, **60**, 141-148.
19. H. W. Goldstein, *J. Phys. Chem.*, 1964, **68**, 39-42.
20. B. McCarroll and D. W. McKee, *Carbon*, 1971, **9**, 301-311.
21. C. Park and D. W. Bogdanoff, *J. Thermophys. Heat Transf.*, 2006, **20**, 487-492.
22. T. Suzuki, K. Fujita, K. Ando and T. Sakai, *J. Thermophys. Heat Transf.*, 2008, **22**, 382-389.
23. L. Zhang, D. A. Pejaković, J. Marschall, M. Dougherty and D. G. Fletcher, *J. Thermophys. Heat Transf.*, 2012, **26**, 10-21.
24. S. Hariharan, M. Majumder, R. Edel, T. Grabnic, S. J. Sibener and W. L. Hase, *J. Phys. Chem. C*, 2018, **122**, 29368-29379.
25. V. Morón, L. Martin-Gondre, P. Gamallo and R. Sayós, *J. Phys. Chem. C*, 2012, **116**, 21482-21488.
26. M. Majumder, K. D. Gibson, S. J. Sibener and W. L. Hase, *J. Phys. Chem. C*, 2018, **122**, 16048-16059.
27. A. Rivero Santamaría, M. Alducin, R. Díez Muiño and J. I. Juaristi, *J. Phys. Chem. C*, 2019, **123**, 31094-31102.

28. J. R. Hahn, H. Kang, S. M. Lee and Y. H. Lee, *J. Phys. Chem. B*, 1999, **103**, 9944-9951.
29. Y.-J. Xu and J.-Q. Li, *Chem. Phys. Lett.*, 2004, **400**, 406-412.
30. C. Janiak, R. Hoffmann, P. Sjovall and B. Kasemo, *Langmuir*, 1993, **9**, 3427-3440.
31. R. Larciprete, P. Lacovig, S. Gardonio, A. Baraldi and S. Lizzit, *J. Phys. Chem. C*, 2012, **116**, 9900-9908.
32. D. Lamoen and B. N. J. Persson, *J. Chem. Phys.*, 1998, **108**, 3332-3341.
33. D. C. Sorescu, K. D. Jordan and P. Avouris, *J. Phys. Chem. B*, 2001, **105**, 11227-11232.
34. A. Incze, A. Pasturel and C. Chatillon, *Surf. Sci.*, 2003, **537**, 55-63.
35. V. Morón, P. Gamallo and R. Sayós, *Theo. Chem. Acc.*, 2011, **128**, 683-694.
36. J. Ito, J. Nakamura and A. Natori, *J. Appl. Phys.*, 2008, **103**, 113712.
37. F. Mehmood, R. Pachter, W. Lu and J. J. Boeckl, *J. Phys. Chem. C*, 2013, **117**, 10366-10374.
38. R. T. Yang and C. Wong, *Science*, 1981, **214**, 437.
39. V. Morón, L. Martin-Gondre, P. Gamallo and R. Sayós, *J. Phys. Chem. C*, 2012, **116**, 13092-13103.
40. T. Sun, S. Fabris and S. Baroni, *J. Phys. Chem. C*, 2011, **115**, 4730-4737.
41. S. C. Xu, H.-L. Chen and M. C. Lin, *J. Phys. Chem. C*, 2012, **116**, 1841-1849.
42. S. G. Srinivasan and A. C. T. van Duin, *J. Phys. Chem. A*, 2011, **115**, 13269-13280.
43. S. Poovathingal, T. E. Schwartzentruber, S. G. Srinivasan and A. C. T. van Duin, *J. Phys. Chem. A*, 2013, **117**, 2692-2703.
44. J. T. Paci and I. Paci, *J. Phys. Chem. C*, 2019, **123**, 29647-29655.
45. B. Jayee, R. Nieman, T. K. Minton, W. L. Hase and H. Guo, *J. Phys. Chem. C*, 2021, **125**, 9795-9808.
46. Y.-J. Xu and J.-Q. Li, *Chem. Phys. Lett.*, 2005, **406**, 249-253.
47. Y. Ma, A. S. Foster, A. Krasheninnikov and R. M. Nieminen, *Phys. Rev. B*, 2005, **72**, 205416.
48. L. Zhechkov, T. Heine and G. Seifert, *Int. J. Quant. Chem.*, 2006, **106**, 1375-1382.
49. M. Wu, E.-Z. Liu and J. Z. Jiang, *Appl. Phys. Lett.*, 2008, **93**, 082504.
50. M. Rubeš, J. Kysilka, P. Nachtigall and O. Bludský, *Phys. Chem. Chem. Phys.*, 2010, **12**, 6438-6444.
51. L. Chen, H. Hu, Y. Ouyang, H. Z. Pan, Y. Y. Sun and F. Liu, *Carbon*, 2011, **49**, 3356-3361.
52. K. Nakada and A. Ishii, *Solid State Commun.*, 2011, **151**, 13-16.
53. Y. Li, J.-C. Ren, R.-Q. Zhang, Z. Lin and M. A. Van Hove, *J. Mat. Chem.*, 2012, **22**, 21167-21172.
54. I. A. Pašti, A. Jovanović, A. S. Dobrota, S. V. Mentus, B. Johansson and N. V. Skorodumova, *Phys. Chem. Chem. Phys.*, 2018, **20**, 858-865.
55. R. Nieman, R. Spezia, B. Jayee, T. K. Minton, W. L. Hase and H. Guo, *J. Chem. Phys.*, 2020, **153**, 184702.
56. Y. Wang, R. Nieman, T. K. Minton and H. Guo, *J. Chem. Phys.*, 2021, **154**, 074708.
57. S. Moon, Y. Hijikata and S. Irle, *Phys. Chem. Chem. Phys.*, 2019, **21**, 12112-12120.
58. P. E. Blöchl, *Phys. Rev. B*, 1994, **50**, 17953-17979.
59. H. J. Monkhorst and J. D. Pack, *Phys. Rev. B*, 1976, **13**, 5188-5192.
60. G. Kresse and J. Furthmuller, *Phys. Rev. B*, 1996, **54**, 11169-11186.
61. G. Kresse and J. Furthmuller, *Comp. Mater. Sci.*, 1996, **6**, 15-50.
62. J. P. Perdew, K. Burke and M. Ernzerhof, *Phys. Rev. Lett.*, 1996, **77**, 3865-3868.

63. J. Klimeš, D. R. Bowler and A. Michaelides, *J. Phys.: Condens. Matter*, 2010, **22**, 022201.
64. J. Heyd, G. E. Scuseria and M. Ernzerhof, *J. Chem. Phys.*, 2003, **118**, 8207-8215.
65. G. Henkelman, B. P. Uberuaga and H. Jónsson, *J. Chem. Phys.*, 2000, **113**, 9901-9904.
66. G. Henkelman and H. Jónsson, *J. Chem. Phys.*, 1999, **111**, 7010-7022.
67. F. López-Urías, J. L. Fajardo-Díaz, A. J. Cortés-López, C. L. Rodríguez-Corvera, L. E. Jiménez-Ramírez and E. Muñoz-Sandoval, *Phys. Chem. Chem. Phys.*, 2020, **22**, 4533-4543.
68. K. Sendt and B. S. Haynes, *Proc. Combus. Inst.*, 2011, **33**, 1851-1858.